Probing Surface Valence, Magnetic Property, and Oxide Ion Diffusion Pathways in B-Site Ordered Perovskite-type $Ba_2Ca_{0.67}M_{0.33}NbO_{6-\delta}$ (M = Mn, Fe, Co)

Wang Hay Kan[a], Pengcheng Dong[a], Jong-Seong Bae[b], Stefan Adams[c], and Venkataraman Thangadurai[*,a]

[a] Department of Chemistry, University of Calgary, 2500 University Drive NW, Calgary, Alberta, Canada T2N 1N4

[b] Division of High Technology Materials Research, Korea Basic Science Institute Busan Center, 1275 Jisa-dong, Gangseo-gu, Busan 618-230, South Korea

[c] Department of Materials Science and Engineering, National University of Singapore, 117575, Singapore

ABSTRACT: Here, we report the valence of transition metals at surface, magnetic ordering and oxide-ion transport pathway of the double perovskite-type $Ba_2Ca_{0.67}M_{0.33}NbO_{6-\delta}$ (M = Mn, Fe, Co). In-situ X-ray photoelectron spectroscopy (XPS) reveals the surface valence for Mn and Co-doped $Ba_2Ca_{0.67}M_{0.33}NbO_{6-\delta}$ are 2.5+ and 2+, respectively at 700 ^{o}C. All the $Ba_2Ca_{0.67}M_{0.33}NbO_{6-\delta}$ samples are paramagnetic with no long-range cooperative interaction between individual spins. Static bond valence sum (BVS), bond valence site energy (BVSE) analyses and molecular dynamics (MD) simulations indicate that oxide ion migration pathways are isotropic in $Ba_2Ca_{0.67}M_{0.33}NbO_{6-\delta}$. In particular, MD simulations (≥ 800 K) show a long-range oxide ion transport with an activation energy of 0.69 eV for $Ba_2Ca_{0.67}Co_{0.33}NbO_{6-\delta}$.

Keyword: in-situ x-ray photoelectron spectroscopy, bond valence sum map, perovskite, defect chemistry

1. INTRODUCTION

Solid oxide fuel cells (SOFCs) are promising energy conversion devices with the highest efficiency among various known fuel cell types, including proton exchange membrane fuel cells, alkaline fuel cells, molten carbonate fuel cells and phosphoric acid fuel cells [1, 2]. Low cost and abundant hydrocarbon fuels (*e.g.,* CH_4) can be electrochemically converted into electricity and heat, while the spent fuels are enriched in CO_2 and they could be sequestrated underground for storage. However, most known Ni-based anodes are suffered from coking under hydrocarbon fuels, and therefore, commercial SOFCs are often equipped with external reformers to improve their durability [3-5]. Over the last two decades, different mixed ion and electronic conductive (MIEC) compounds were investigated as alternative SOFCs anodes, as some showed improved chemical stability with hydrocarbons containing ppm level H_2S impurity [1, 6-12]. Among them, perovskite- and fluorite-type metal oxides are the most popular structures being studied due to their high total electrical conductivity (*e.g.,* 0.12 S cm^{-1} for $Ce_{0.9}Gd_{0.1}O_{1.9}$ at 750 ^{o}C and 0.04 S cm^{-1} for $Ba_2Ca_{0.79}Co_{0.5}Nb_{0.71}O_{6-\delta}$ at 800 ^{o}C) and amenable for chemical doping [6-9,13]. Nonetheless, the reaction mechanism of the electrochemical reactions occurred on the MIEC surfaces are not well understood. A detailed analysis on the change of surface valences at different temperatures/atmospheres could help to better understand and to more efficiently control the kinetics of the electrochemical reactions in SOFCs and other solid-state ionic devices.

Recently, the concentration of Ce^{3+} near the surface of fluorite-type CeO_2 was found to be about two orders of magnitudes higher than that in the bulk, as revealed by *in-situ* X-ray photoelectron spectroscopy (XPS) [14-18]. Moreover, the concentration of low valence Ce^{3+} ions was hardly altered upon changing the temperature and applied potential [14,16]. Recently, Kan *et al.* reported the valance of Fe at surface level of a double perovskite-type $Ba_2Ca_{0.67}Fe_{0.33}NbO_{6-\delta}$ using multiplet fitting on the variable temperature *in-situ* XPS data [4]. The low valence Fe^{2+} ions at the surface was found to be about three times higher than the bulk sample in air obtained from thermo-gravimetric and chemical titration method. This finding suggests that the coordination number of cations (MO_8 in fluorite vs. MO_6 in perovskite) in the bulk seems to play a crucial role to the surface valence state. Previous studies of doped $La_{1-x}Sr_xTiO_3$ have indicated that there seems to be a connection between the surface reaction of MIEC and oxide-ion conduction [19]. However, the mechanism processes are not well understood, and more in-situ studies are required to unravel some keys properties of MIECs. Here, we report the valence of Mn and Co ions at surface level in double perovskite-type $Ba_2Ca_{0.67}M_{0.33}NbO_{6-\delta}$ (M = Mn, Co) using *in-situ* XPS. In addition, we also analyzed the magnetic susceptibility of $Ba_2Ca_{0.67}M_{0.33}NbO_{6-\delta}$ (M = Mn, Fe, Co) to understand the spin configuration/ordering. Lastly, for the first time, the oxide-ion migration in $Ba_2Ca_{0.67}M_{0.33}NbO_{6-\delta}$ was studied using both the conventional bond valence sum (BVS) [20, 21], and the more recent bond valence site energy (BVSE) methods [22, 23]. This work may help to design the next generation MIECs with higher electrochemical activity and enhanced chemical stability.

2. EXPERIMENTAL SECTION

2.1 Synthesis. Double perovskite-type of the nominal chemical compositions $Ba_2Ca_{0.66}M_{0.33}NbO_{6-\delta}$ (M = Mn, Fe, Co) was synthesized by conventional ceramic method [4, 7-9]. Stoichiometric amounts of ACS-grade (99+%) $Ba(NO_3)_2$, $CaCO_3$, Nb_2O_5, $MnCO_3$, Fe_2O_3 and $Co(NO_3)_2{\cdot}6H_2O$ were ball-milled in a Planetary Mono Mill (Pulverisette, Fritsch, Germany), using 2-propanol as solvent and ZrO_2 balls, for 6 h at 200 rpm with reversed rotation every hour. The precursors were dried and sintered at 1000 ^oC (5 ^oC/min) in air for 12 h. The resulting powders were hand-grinded and pressed into pellets using isostatic pressure of 200M Pa and sintered at 1400 ^oC (5 ^oC/min) in air for 12 h.

2.2 Characterization. Solid phase purity was confirmed using a Bruker D8 Advance powder X-ray diffractometer (Cu K_α, 40 kV, 40 mA). Variable temperature *in-situ* X-ray photoelectron spectra (XPS) were recorded using a Thermo Fisher Scientific Theta Probe XPS (UK). Theta Probe XPS system used monochromated Al Kα x-ray source (hν = 1486.6 eV) at a spot size of 400 μm in diameter with charge compensation. Emitted photoelectrons were detected by a multichannel detector at take off angle of 90^o

relative to the sample surface. Seah and Dench suggested that the penetration depth of XPS depends upon the material and the kinetic energy of the electron being measured [24]. As heavier atoms have lower penetration depth due to their stronger absorbance of X-ray radiation, the anticipated penetrations of ca. 5-10 nm for the investigated compounds since they have heavier elements than standard Si. To study the change of the oxidation state for the surface valences for sample was subjected to thermal annealing in the analysis chamber. Before measurement, the sample has been kept in the load lock chamber overnight, and then it was transferred to the analysis chamber for surface analysis and variable temperature dependent measurement. The XPS spectra were acquired at sample temperature of 25, 300, 500, 600, and 700 ^{o}C, upon manually heating in step of 25 ^{o}C, at the base pressure 4 x 10^{-9} mbar, 1 x 10^{-8} mbar, 5 x 10^{-8} mbar, 8 x 10^{-8} mbar and 1 x 10^{-7} mbar, respectively. Hydrocarbon and moisture contained in the sample were outgassing with increasing temperature so that vacuum level was increased in the chamber. In order to allow the vacuum to recover after each temperature rise the sample was kept at that temperature for 30 minutes before starting the measurement. During the measurements, the base pressure in the turbo-pumped analysis chamber was at 4×10^{-9} mbar. Survey spectra were obtained at pass energy of 300 eV and at a step energy of 1 eV. High-resolution spectra were acquired at a pass energy of 50 eV and at a step energy of 0.1 eV. All of the obtained binding energy (BEs) values were compensated with that of the adventitious carbon (C1s) core level peak at 284.8 eV as a reference. CasaXPS (ACADEMIC) was used to analyze the data.

The valence of Mn and Co in the bulk samples at ambient condition was determined by iodometric titration [4, 7]. A small amount of samples (ca. 10 mg) was first dissolved using dilute HCl. This step was to ensure that all transition metal cations became $M(H_2O)_6^{n+1}$ ions in aqueous solution. The solution was then reacted with KI to reduce the transition metal ions:

$$2I^{-} + 2M^{n+1} \rightarrow I_2 + 2M^{n+} \quad (1)$$

To avoid lower valent $M(H_2O)_6^{n+}$ ions from re-oxidation in air, the reactions were conducted under CO_2. The concentration of I_2 was determined by a standardized sodium thiosulfate solution using starch solution as an indicator:

$$I_2 + 2S_2O_3^{2-} \rightarrow 2I^- + S_4O_6^{2-} \qquad (2)$$

Once the valence state at 25 °C was determined, the valence state was calculated by from the weight loss at elevated temperatures which was contributed by the formation of oxide-ion vacancy:

$$2O^{2-} \rightarrow O_2 + 4e^- \qquad (3)$$

The magnetic susceptibility was measured by a superconducting quantum interference device (SQUID) magnetometer. Field cooled (FC) measurements were obtained by cooling the samples from 300 to 1.9 K in the presence of applied field (1000 Oe).

Bond valence sum map was calculated from 3DBVSMAPPER [25]. The imported crystallographic information (CIF) files were obtained from the Rietveld refinement of PXRD patterns of $Ba_2Ca_{0.67}M_{0.33}NbO_{6-\delta}$ [6, 7, 9]. The valences of Mn, Fe, and Co ions were assumed to be 2+, 3+ and 2+ in the calculations, respectively. For the bond valence site energy calculation, a 2 × 2 × 3 supercell of the $Ba_2Ca_{0.667}Co_{0.333}NbO_{6-\delta}$ structure was created from the PXRD structure data with idealized stoichiometry $Ba_{96}Ca_{32}Co_{16}Nb_{48}O_{264}$, where both the Ca:M and the oxygen vacancy distribution was, in the absence of definitive information on cation ordering, initially random. The oxygen vacancy distribution has been relaxed by a series of molecular dynamics (MD) simulations at temperatures 1400 K down to 300 K using the bond valence-based *softBV* force field parameters [23]. Starting from this geometry-optimized structure with the relaxed lattice parameters at 300K, a static model of oxygen anion site energies has been calculated for a grid spanning the supercell with a resolution of $(0.1Å)^3$ using the softBV software suite developed in the group of one of us. Moreover, a series of NVT MD simulations has been conducted using the same Morse-type *softBV* parameters and the software package GULP [26]. At each temperature in the range 400 K < T < 1400 K, the unit cell volume was relaxed to achieve a pressure of 0 ± 0.1 GPa. At each temperature, an NVT equilibration run of 50 – 200 ps was conducted followed by a production run using a time step of 1fs for simulations at T ≥ 700 K, and of 1.25 fs below 700 K. The simulations were conducted starting from 1400 K to 400 K where the final state of each calculation was obtained and used for to the next run.

3. RESULTS AND DISCUSSION

3.1 Surface Valence of Transition Metals in $Ba_2Ca_{0.67}M_{0.33}NbO_{6-\delta}$ (M = Mn, Co). Generally, electrochemical reactions are known to happen on interfaces of a sample, and therefore, the XPS analysis of valence at the surface level could provide some insight (e.g., concentration of electrochemically active metal ions) of the reaction mechanism [1]. However, the exact penetration depth is very challenging to be quantified, as mean free path of X-ray changes as a function of sample porosity and atomic mass of elements. As shown in Figure 1, the binding energies of all elements in $Ba_2Ca_{0.67}M_{0.33}NbO_{6-\delta}$ could be indexed based on the peaks' positions reported in the National Institute of Standards and Technology (NIST) database [27]. The elemental ratio was obtained by integrating the corresponding peaks' areas and the results are summarized in Table 1. The cation ratio was found to be consistent with the chemical formulas of all compounds in different temperatures, except for the Co-based spectra at 25 ^{o}C that had poor peak resolution due to the adventitious carbon on the sample surface. Such impurity species were removed in the higher temperature spectra, as the adventitious carbon is only weakly bonded (van der Waals). Similar to our previous study, the oxygen signal was over-estimated which may be due to adventitious CO_x and other impurities in the atmosphere [4].

The valence of compounds was further studied using the Gupta and Sen (GS) multiplet-structural fitting and other de-convolution technique of the variable temperature *in-situ* X-ray photoelectron spectra. One of the main reasons to consider the multiplet-structure is that species with unpaired electron may interact with an electron vacancy in the core during the X-ray photoelectron process [28, 29]. McIntrye, Biesinger and Grosvenor reported detailed multiplet-structural parameters of the various cations in the first row transition metal compounds [30-33]. Comparing to the earlier reported case of Fe ions, the fitting of Mn ions was more challenging since many stable oxidation states had been reported, ranging from 0 to +7. In addition, high spin Mn^{3+} ions have d^4 configuration and are susceptible to disproportional reaction to form Mn^{2+} and Mn^{4+} species at elevated temperatures [34-39]. Our fitting models were constructed based on Biesinger's XPS analysis of first row transition metal oxides and hydroxides [30]. Thus, the Mn^{2+} ion in $Ba_2Ca_{0.67}Mn_{0.33}NbO_{6-\delta}$ was fitted with six main peaks with peak positions between 640 to 647 eV and the full width at half maximum (FWHM) of 1.21-1.23 eV was used for the $2p_{3/2}$ spectra (Figure 2). An additional stake-up peak with FWHM of 3.5 eV was also included, as recommended by Biesinger and coworkers [30, 40]. The six peak positions were constrained to be X, X + 1, X + 1.9, X + 2.9, X + 4 and X + 5.75 where X was allowed to change within the above peak position constraint (*i.e.,* 640-647 eV). Similarly, the multiplet structures for Mn^{3+} and Mn^{4+} ions were constructed with use of five and six peaks, respectively. The background was modeled with Shirley-type algorithm for all spectra, and the peak shape was fitting with Gaussian-Lorentzian line shape GL30. All other parameters were allowed to change until the convergence was reached. The detailed peak positions, widths and relative intensities are summarized in Table 2. High spin $2p_{3/2}$ of Mn^{2+}, Mn^{3+} and Mn^{4+} species were quantified in term of binding energy (eV), percentage of total energy, FWHM value (eV) and spectral component separation (eV). The resident standard deviations (STD) of 500-700 ^{o}C were 1.21, 0.87 and 0.97, respectively (Table 2). At 500 ^{o}C, the average surface valence of Mn ions was found to be ca. 2.6+ (44.5% Mn^{2+}, 50.7% Mn^{3+} and 4.6% Mn^{4+}). As temperature increased, the average surface valence decreased slightly to ca. 2.5+ mainly because of the reduction of Mn^{3+} and Mn^{4+} species at elevated temperatures (Figure 2).

In contrast to the Mn 2p spectra, the Co 2p overlapped strongly with the Ba 3d spectra with peak position between 778 and 785 eV. As a result, a simple fitting approach was applied to analyze the valence state of Co from the 3p (55-65) spectra and O 1s spectra for the whole temperature range [41, 42]. A satellite peak with higher binding energy was also considered due to a multi-electron excitation for all 3p spectra [32]. For Co ions, the surface valence was ca. 2+ based on 3p spectra (Figure 3). Table 3 lists the curve-fitting parameters for Co 3p and O 1s spectra in $Ba_2Ca_{0.67}Co_{0.33}NbO_{6-\delta}$. The binding energy (eV), percentage of total energy, FWHM value (eV) and spectral component separation (eV) were all quantified as a function of temperature. The resident standard deviation (STD) of 500, 600 and 700 ^{o}C data was found to be 0.88, 0.95 and 0.84, respectively.

The peak positions were found to be slightly smaller than the values reported by Mclntyre *et al*[30]. Such a difference can be explained by a reduced shielding effect (blue-shift) at elevated temperature. The peak positions were found to be nearly unchanged as temperature increased from 500 to 700 ^{o}C. Such information indicated that the valence was insensitive to the temperature. The O 1s spectra showed two peaks, which can be described as lattice and defective oxygen species (Figure 4) and they were consistent to the peak position of CoO [30, 32, 40]. Quite interestingly, due to the complication of multiple valences (2+ 3+, and 4+) of Mn ions, it appears that only Mn^{3+} and Mn^{4+} ions were reduced at high temperatures. As a comparison between the bulk and surface valences, Co species showed similar behavior as the Fe analog in which lower surface valence was found. But, the former one was less temperature sensitive (Figures 5 and 6). We speculated that the higher than expected surface valence of Mn ions would be due to the BaO surface segregation and forming A-site deficient perovskite $A_{1-x}BO_3$ [43].

3.2. Magnetic Susceptibility of $Ba_2Ca_{0.67}M_{0.33}NbO_{6-\delta}$. Determination of the magnetic properties in solid-state materials is crucial to understand the crystal structure, spin configuration and valence state [44-48]. An excellent example is that the cubic $LiMn_2O_4$ (space group *Fd-3m*) was found to be antiferromagnetic with a Weiss constant of -266 K for the $Mn^{3.5+}$ ions [49]. The spin configuration is temperature dependent due to Curie-Weiss law in which paramagnetic state can be converted into ferromagnetic, antiferromagnetic or ferromagnetic state at low temperature regime [50]. Therefore, the molar magnetic moment should be measured to evaluate the spin configuration.

As shown in Figure 7, the inversed magnetic susceptibility χ passed through zero at low temperature regime, indicating that the investigated compounds were paramagnetic for the whole temperature range. Three main reasons can be accounted why the spin in the 3d orbitals were not coupled with each other. First of all, the concentration of transition metal ions in the B-site is about 17% occupancy. The low occupancy reduced the interaction between the metal ions E_g and oxygen 2p orbitals. Second, the presence of diamagnetic Ca^{2+} and Nb^{5+} in the B-site could also interrupt the long-range spins cooperative interaction between individual spins. Lastly, the investigated samples had up to ~ 10% oxide-ion vacancies in the perovskite and may further reduce the orbital interaction.

3.3. Oxide-ion Transport Pathways in $Ba_2Ca_{0.67}M_{0.33}NbO_{6-\delta}$. An experimental determination of ion migration pathways typically requires high quality single crystal data that allow for a reliable expansion of higher order anharmonic atomic displacement parameters, or – with higher experimental uncertainties - powder neutron diffraction data of sufficient quality for a maximum entropy analysis [51, 52]. Still any diffraction method can in a cation-disordered method only yield averaged results for an oxide ion pathway. Brown, Adams and Avdeev developed a facile methodology in which the bond valence of the targeted mobile ion can be derived from its crystal structure based on the hypothesis that the mobile ions will preferentially travel along pathways of lowest energy [53-56]. While the method has been applied widely to study cation migration pathways [53], it has only occasionally been applied to anion conductors [54, 55]. Regions of low valence mismatch could be connected to form iso-surfaces and they can be correlated to the ionic diffusion pathways in solid conductors [20, 21, 25, 56, 57]. Traditionally, the individual bond valence of an atom/a point can be calculated from the bond length, number of bonds, and oxidation state. Herein, the bond valence values were calculated (by 3DBVSMAPPER) over three-dimensional grids of unit cell using cell parameter [25], atomic position, atomic occupancy and valence state of atoms, as input parameters. The bond valence mismatches for the oxide-ion in $Ba_2Ca_{0.67}M_{0.33}NbO_{6-\delta}$ are shown in Figure 8(a-b). For simplification, the valences of Mn, Fe, and Co ions were assumed to be 2+, 3+ and 2+ in the calculations, respectively. The oxide-ion vacancy was taken into account and it was calculated based on the charge-balance of all ions in the formula of samples. The regions of low valence mismatch form a percolating migration path for bond valence mismatches ~ 0.4 v.u. in the all investigated perovskites. Although the compounds had different valence state for transition metal ions and oxide-ion vacancy in the unit cells, similar isosurfaces were observed.

These bond valence sum mismatch isosurface plots clarify that the regular oxygen positions are the only possible sites for oxide ions, and thus the transport mechanism is a vacancy mechanism. Due to the cubic symmetry of the investigated compounds, the ionic conduction pathway is isotropic. For all BVS map analyses, however, the migration barrier estimation in bond valence units cannot be verified to any experimental data. In addition, no the structural disorder was taken into the analysis for consideration. Hence, the BVS calculations for $Ba_2Ca_{0.67}Co_{0.33}NbO_{6-\delta}$ have been complemented by static BVSE calculation of a representative local structure model and molecular dynamics (MD) simulations of a relaxed $2 \times 2 \times 3$-fold supercell. Isosurfaces of constant oxide ion site energy in the supercell (Figure 8c) harmonize with the BVS mismatch isosurfaces. The regular O sites along Nb-O-Ca/M connecting lines are found to be the only possible low energy sites, but the energy-scaled BVSE approach permits us to predict the migration barriers for long-range oxide ion motion to ca. 0.7 eV. Interestingly, local oxide ion motion can occur with considerably smaller activation energy of ca. 0.25 eV, but this motion is restricted to hops between occupied and vacant oxide ion sites within the same NbO_x coordination polyhedron. This indicates that the Nb-O bond is considerably stronger than the bonds to the divalent cations (Ca or Co and Ba) in the first coordination shell of the oxide ion and tends to be preserved in low energy hops.

NVT MD simulations for the $Ba_{96}Ca_{32}Co_{16}Nb_{48}O_{264}$ structure model using the same Morse-type *softBV* parameters for the temperature range 400 K < T < 1400 K underline the suitability of the parameter set, as the relaxed room temperature lattice parameter of a = 8.367 Å is just 0.1% smaller than the experimental value of 8.375 Å and the linear variation of the relaxed lattice parameters with temperature corresponds to a thermal expansion coefficient of 2×10^{-5} K^{-1}. MD simulations at temperatures ≥ 800 K show a long range O^{2-} transport with an activation energy of 0.69 eV (see filled symbols in Figure 9). For lower temperatures the simulations did not yield a quantifiable long-range oxide ion transport over the up to 12500 ps of the simulation runs. Instead the limiting slopes of the mean square displacement vs. time curves for these temperatures (and for intermediate time domains in the high temperature simulations) formally correspond to an activation energy of 0.24 eV (crosses in Figure 9) again in remarkable agreement with the predictions form the BVSE model. From visual inspection of the trajectories it was clarified that these hops correspond to localized oxide ion hops within NbO_x coordination polyhedral confirming the predictions of the static BVSE model. It should be noted that while Figure 9 displays the conductivity data in a log(σ) vs. 1000/T plot to yield a direct overview of the observed conductivities, the activation energy value was derived from a corresponding log(σT) vs. 1000/T plot.

The two different activation energies for oxide ion motions within and out of a NbO_x coordination polyhedron should not be misunderstood as two different oxide ion species of different local mobility. The difference simply arises from the strength of the cation-oxygen bond that has to be broken during the hop and obviously a hop involving the breaking of a Nb^{5+}-O bond will require a higher energy than a hop that preserves Nb^{5+}-O bond and instead breaks weaker bonds with a divalent cation. As a consequence from these findings, it is expected that for this stoichiometry local ion mobility probes such as NMR studies will find a considerably lower activation energy for oxide ion diffusion than dc conductivity measurements, and that the lower migration energy barrier for the local hops constitutes a lower limit to the achievable activation energy when varying the oxygen vacancy concentration.

4. CONCLUSIONS

The surface valence state of Mn and Co in $Ba_2Ca_{0.67}M_{0.33}NbO_{6-\delta}$ (M = Mn, Fe, Co) was studied by *in-situ* XPS. The surface valence of Co and Mn ions was found to be insensitive between 500 and 700 ^{o}C. The surface valences of Mn and Co were determined to be 2.5+ and 2+, respectively, at 700 ^{o}C. All investigated $Ba_2Ca_{0.67}M_{0.33}NbO_{6-\delta}$ were paramagnetic from room temperature down to 1.9 K with no long-range spin coupling. Bond valence site energy calculation and molecular dynamics simulation with bond-valence based empirical force fields show the 3D percolating migration path for the investigated perovskite $Ba_2Ca_{0.67}Co_{0.33}NbO_{6-\delta}$. The pathway is insensitive to the change of valence of the transition metal ions and an oxide-ion percolation network could explain the rise of electrochemical activity of the transition metal-doped $Ba_2Ca_{0.67}M_{0.33}NbO_{6-\delta}$.

Corresponding Author
* Email: vthangad@ucalgary.ca; Phone: 1 403 210 8649

ACKNOWLEDGMENT

This research was supported through funding to the NSERC Solid Oxide Fuel Cell Canada Strategic Research Network and other sponsors listed at www.sofccanada.com. W. H. K. thanks Alberta Innovates – Technology Futures (AITF) for graduate scholarship. We appreciate Dr. Simon Trudel for his help with magnetic measurements in University of Calgary. We also thank Drs. Mark Biesinger in University of Western Ontario and Andrew Grosvenor from University of Saskatchewan for the helpful discussion about XPS fitting analysis. We thank Dr. Zachary Moorhead-Rosenberg in University of Texas at Austin for analyzing the magnetic data, and Haomin Chen in National University of Singapore in preparing BVSE maps. S.A. would like to thank the National Research Foundation, Prime Minister's Office, Singapore for support in developing the BVSE method under its Competitive Research Program (CRP Awards NRF-CRP 10-2012-6 and NRF-CRP 8-2011-4).

REFERENCES

[1] A. Atkinson, S. Barnett, R.J. Gorte, J.T.S. Irvine, A.J. McEvoy, M. Mogensen, S.C. Singhal, J. Vohs, Nat. Mater., 3 (2004) 17.

[2] A.J. Jacobson, Chem. Mater., 22 (2010) 660.

[3] John T. S. Irvine, D.C. Sinclair, A.R. West, Adv. Mater., 2 (1990) 132.

[4] W.H. Kan, M. Chen, J.-S. Bae, B.-H. Kim, V. Thangadurai, J. Mater. Chem. A, 2 (2014) 8736.

[5] A. Orera, P.R. Slater, Chem. Mater., 22 (2010) 675.

[6] W.H. Kan, J. Lussier, M. Bieringer, V. Thangadurai, Inorg. Chem., 53 (2014) 10085.

[7] W.H. Kan, M. Roushanafshar, A. Vincent, T. Fuerstenhaupt, M. Parvez, J. Luo, V. Thangadurai, RSC Adv., 3 (2013) 23824.

[8] W.H. Kan, T.T. Trinh, T. Furstenhaupt, V. Thangadurai, ECS Trans., 35 (2011) 1259.

[9] W.H. Kan, T.T. Trinh, T. Furstenhaupt, V. Thangadurai, Can. J. Chem., 89 (2011) 688.

[10] Y.-H. Huang, G. Liang, M. Croft, M. Lehtimaki, M. Karppinen, J.B. Goodenough, Chem. Mater., 21 (2009) 2319.

[11] D. Neagu, J.T.S. Irvine, Chem. Mater., 22 (2010) 5042.

[12] S. Tao, J.T.S. Irvine, Chem. Mater., 16 (2004) 4116.

[13] M.G. Chourashiya, J.Y. Patil, S.H. Pawar, L.D. Jadhav, Mater. Chem. Phys., 109 (2008) 39.

[14] W.C. Chueh, A.H. McDaniel, M.E. Grass, Y. Hao, N. Jabeen, Z. Liu, S.M. Haile, K.F. McCarty, H. Bluhm, F. El Gabaly, Chem. Mater., 24 (2012) 1876.

[15] Z.A. Feng, M.L. Machala, W.C. Chueh, Phys. Chem. Chem. Phys., 17 (2015) 12273.

[16] C. Zhang, M.E. Grass, A.H. McDaniel, S.C. De Caluwe, F. El Gabaly, Z. Liu, K.F. McCarty, R.L. Farrow, M.A. Linne, Z. Hussain, G.S. Jackson, H. Bluhm, B.W. Eichhorn, Nat. Mater., 9 (2010) 944.

[17] C. Zhang, M.E. Grass, Y. Yu, K.J. Gaskell, S.C. DeCaluwe, R. Chang, G.S. Jackson, Z. Hussain, H. Bluhm, B.W. Eichhorn, Z. Liu, ACS Catal., 2 (2012) 2297.

[18] C. Zhang, Y. Yu, M.E. Grass, C. Dejoie, W. Ding, K. Gaskell, N. Jabeen, Y.P. Hong, A. Shavorskiy, H. Bluhm, W.-X. Li, G.S. Jackson, Z. Hussain, Z. Liu, B.W. Eichhorn, J. Am. Chem. Soc., 135 (2013) 11572.

[19] J.C. Ruiz-Morales, J. Canales-Vázquez, C. Savaniu, D. Marrero-López, W. Zhou, J.T.S. Irvine, Nature, 439 (2006) 568.

[20] S. Adams, R.P. Rao, Phys. Status Solidi A, 208 (2011) 1746.

[21] V. Thangadurai, S. Adams, W. Weppner, Chem. Mater., 16 (2004) 2998.

[22] S. Adams, R. Prasada Rao, Solid State Ionics, 184 (2011) 57.

[23] S. Adams, R.P. Rao, Understanding Ionic Conduction and Energy Storage Materials with Bond-Valence-Based Methods, in: I.D. Brown, K.R. Poeppelmeier (Eds.) Bond Valences, Springer Berlin Heidelberg, 2014, pp. 129.

[24] M.P. Seah, W.A. Dench, Surf. Interface Anal., 1 (1979) 2.

[25] M. Sale, M. Avdeev, J. Appl. Crystallogr., 45 (2012) 1054.

[26] J.D. Gale, J. Chem. Soc., Faraday Trans., 93 (1997) 629.

[27] C.D. Wagner, A.V. Naumkin, A. Kraut-Vass, J.W. Allison, C.J. Powell, J.R.J. Rumble, in, 2003.

[28] R.P. Gupta, S.K. Sen, Phys. Rev. B, 12 (1975) 15.

[29] R.P. Gupta, S.K. Sen, Phys. Rev. B, 10 (1974) 71.

[30] M.C. Biesinger, B.P. Payne, B.R. Hart, A.P. Grosvenor, N.S. McIntryre, L.W.M. Lau, R.S.C. Smart, J. Phys.: Conf. Ser., 100 (2008) No pp. given.

[31] A.P. Grosvenor, B.A. Kobe, M.C. Biesinger, N.S. McIntyre, Surf. Interface Anal., 36 (2004) 1564.

[32] N.S. McIntyre, M.G. Cook, Anal. Chem., 47 (1975) 2208.

[33] N.S. McIntyre, D.G. Zetaruk, Anal. Chem., 49 (1977) 1521.

[34] P.G. Bruce, A.R. Armstrong, R.L. Gitzendanner, J. Mater. Chem., 9 (1999) 193.

[35] Y.-I. Jang, B. Huang, H. Wang, D.R. Sadoway, Y.-M. Chiang, J. Electrochem. Soc., 146 (1999) 3217.

[36] S.K. Mishra, G. Ceder, Phys. Rev. B: Condens. Matter Mater. Phys., 59 (1999) 6120.

[37] E. Pollert, S. Krupicka, E. Kuzimicova, J. Phys. Chem. Solids, 43 (1982) 1137.

[38] L. Pinsard, J. Rodriguez-Carvajal, A. Revcolevschi, J. Alloys Compd., 262-263 (1997) 152.

[39] Y.J. Lee, F. Wang, C.P. Grey, J. Am. Chem. Soc., 120 (1998) 12601.

[40] M.C. Biesinger, B.P. Payne, A.P. Grosvenor, L.W.M. Lau, A.R. Gerson, R.S.C. Smart, Appl. Surf. Sci., 257 (2011) 2717.

[41] G.C. Allen, S.J. Harris, J.A. Jutson, J.M. Dyke, Appl. Surf. Sci., 37 (1989) 111.

[42] A.B. Mandale, S. Badrinarayanan, S.K. Date, A.P.B. Sinha, J. Electron Spectrosc. Relat. Phenom., 33 (1984) 61.

[43] J. Druce, H. Tellez, M. Burriel, M.D. Sharp, L.J. Fawcett, S.N. Cook, D.S. McPhail, T. Ishihara, H.H. Brongersma, J.A. Kilner, Energy & Environmental Science, 7 (2014) 3593.

[44] A.J. Hauser, J.M. Lucy, H.L. Wang, J.R. Soliz, A. Holcomb, P. Morris, P.M. Woodward, F.Y. Yang, Appl. Phys. Lett., 102 (2013) 032403/1.

[45] P. Karen, A.R. Moodenbaugh, J. Goldberger, P.N. Santhosh, P.M. Woodward, J. Solid State Chem., 179 (2006) 2120.

[46] R.A. Ricciardo, A.J. Hauser, F.Y. Yang, H. Kim, W. Lu, P.M. Woodward, Mater. Res. Bull., 44 (2009) 239.

[47] A.E. Taylor, R. Morrow, D.J. Singh, S. Calder, M.D. Lumsden, P.M. Woodward, A.D. Christianson, Phys. Rev. B: Condens. Matter Mater. Phys., 91 (2015) 1.

[48] T. Vogt, P.M. Woodward, P. Karen, B.A. Hunter, P. Henning, A.R. Moodenbaugh, Phys. Rev. Lett., 84 (2000) 2969.

[49] C. Masquelier, M. Tabuchi, K. Ado, R. Kanno, Y. Kobayashi, Y. Maki, O. Nakamura, J.B. Goodenough, J. Solid State Chem., 123 (1996) 255.

[50] A.R. West, Solid State Chemistry and its Applications, John Wiley and Sons, 1984.

[51] S.-i. Nishimura, G. Kobayashi, K. Ohoyama, R. Kanno, M. Yashima, A. Yamada, Nat. Mater., 7 (2008) 707.

[52] J. Han, J. Zhu, Y. Li, X. Yu, S. Wang, G. Wu, H. Xie, S.C. Vogel, F. Izumi, K. Momma, Y. Kawamura, Y. Huang, J.B. Goodenough, Y. Zhao, Chem. Commun. (Cambridge, U. K.), 48 (2012) 9840.

[53] M. Avdeev, M. Sale, S. Adams, R.P. Rao, Solid State Ionics, 225 (2012) 43.

[54] S. Adams, E.S. Tan, Solid State Ionics, 179 (2008) 33.

[55] S. Adams, Solid State Ionics, 177 (2006) 1625.

[56] I.D. Brown, Chem. Rev. (Washington, DC, U. S.), 109 (2009) 6858.

[57] K. Fujii, Y. Esaki, K. Omoto, M. Yashima, A. Hoshikawa, T. Ishigaki, J.R. Hester, Chem. Mater., 26 (2014) 2488.

Table 1. X-ray Photoelectron Spectroscopy (XPS) Elemental Analysis of the Near-Surface (~5-10 nm) Composition of $Ba_2Ca_{0.67}M_{0.33}NbO_{6-\delta}$ (M = Mn and Co) from 25-700 ^{o}C.

$Ba_2Ca_{0.67}Mn_{0.33}NbO_{6-\delta}$					
Temperature (^{o}C)	Ba3d	Ca2p	Mn2p	Nb3p	O1s
25	1.85	0.65	0.33	1.01	8.97
300	2.01	0.68	0.33	1.01	6.48
500	2.04	0.65	0.33	0.98	6.31
600	1.96	0.62	0.33	1.06	6.23
700	2.08	0.65	0.33	1.01	5.85
Theoretical	2.02	0.68	0.33	1.01	5.61
$Ba_2Ca_{0.67}Co_{0.33}NbO_{6-\delta}$					
Temperature (^{o}C)	Ba3p	Ca2p	Co3s	Nb3p	O1s
25	2.02	0.58	0.33	0.73	6.60
300	1.80	0.51	0.33	0.86	5.72
500	1.87	0.61	0.33	0.95	5.82
600	1.98	0.65	0.33	1.03	6.36
700	1.84	0.63	0.33	0.93	5.50

Table 2. Gupta and Sen (GS) Multiplet Parameters for the Mn 2p Spectra in $Ba_2Ca_{0.67}Mn_{0.33}NbO_{6-\delta}$.

Temperature (°C)	Ions	Peak 1 (eV) [FWHM]	%	Peak 2 (eV) [FWHM]	%	Peak 3 (eV) [FWHM]	%	Peak 4 (eV) [FWHM]	%	Peak 5 (eV) [FWHM]	%	Peak 6 (eV) [FWHM]	%
500	Mn^{2+}	640.1 [1.2]	10.6	641.1 [1.2]	12.4	642.0 [1.2]	9.8	642.9 [1.2]	5.6	644.1 [1.2]	2.1	645.8 [3.5]	4.1
	Mn^{3+}	640.7 [1.8]	9.6	641.8 [1.8]	22.6	643.1 [1.7]	12.8	644.6 [1.8]	4.3	646.2 [1.7]	1.6		
	Mn^{4+}	641.8 [0.8]	1.9	642.6 [0.9]	1.2	643.3 [0.8]	0.7	644.1 [0.8]	0.4	644.9 [0.9]	0.2	645.9 [0.8]	0.1
600	Mn^{2+}	640.2 [1.2]	12.5	641.1 [1.2]	14.4	642.1 [1.2]	11.5	643.0 [1.2]	6.5	644.1 [1.2]	2.4	645.9 [3.5]	4.7
	Mn^{3+}	640.8 [1.8]	8.9	641.9 [1.8]	21.0	643.1 [1.7]	11.9	644.6 [1.7]	4.0	646.3 [1.8]	1.5		
700	Mn^{2+}	640.5 [1.2]	12.3	641.4 [1.2]	14.2	642.4 [1.2]	11.3	643.3 [1.2]	6.4	644.5 [1.2]	2.4	646.2 [3.5]	4.7
	Mn^{3+}	641.1 [1.8]	9.2	642.2 [1.7]	21.6	643.4 [1.8]	12.3	644.9 [1.7]	4.1	646.6 [1.8]	1.5		

Table 3. Curve-fitting Parameters for Co 3p and O 1s Spectra in $Ba_2Ca_{0.67}Co_{0.33}NbO_{6-\delta}$.

Temperature (^oC)	Species	$3p_{3/2}$ Peak (eV) [FWHM]	Species	$s_{1/2}$	Peak (eV) [FWHM]	%
500	Co^{2+}	59.5 [4.2]	O (lattice)	1s	529.2 [1.9]	90
	Co^{2+} satellite	64.2 [3.0]	O (defect)	1s	532.0 [1.7]	9
600	Co^{2+}	59.7 [4.3]	O (lattice)	1s	529.3 [2.0]	88
	Co^{2+} satellite	64.4 [4.1]	O (defect)	1s	532.1 [2.0]	11
700	Co^{2+}	59.5 [4.3]	O (lattice)	1s	529.4 [2.1]	48
	Co^{2+} satellite	64.2 [3.4]	O (defect)	1s	532.2 [2.0]	51

Figure Captions

Figure 1. X-ray photoelectron spectroscopy (XPS) elemental analysis of the near-surface of (a) $Ba_2Ca_{0.67}Mn_{0.33}NbO_{6-\delta}$ and (b) $Ba_2Ca_{0.67}Co_{0.33}NbO_{6-\delta}$ from 25-700 ^oC.

Figure 2. Multiplet curve-fitting of Mn $2p_{3/2}$ spectra at (a) 500 ^oC, (b) 600 ^oC and (c) 700 ^oC.

Figure 3. Curve-fitting of Co^{2+} $3p_{3/2}$ spectra at (a) 500 ^oC, (b) 600 ^oC and (c) 700 ^oC.

Figure 4. Curve-fitting of O $1s_{1/2}$ spectra at (a) 500 ^oC, (b) 600 ^oC and (c) 700 ^oC.

Figure 5. Bulk (air and H_2) and surface (air) valences of (a) $Ba_2Ca_{0.67}Mn_{0.33}NbO_{6-\delta}$ and (b) $Ba_2Ca_{0.67}Co_{0.33}NbO_{6-\delta}$ from 500-700 ^oC.

Figure 6. Thermogravimetric analysis (TGA) of $Ba_2Ca_{0.67}M_{0.33}NbO_{6-\delta}$ (M = Mn, Fe, Co) in air and H_2.

Figure 7. Field-cooled (FC) measurements for powdered samples of $Ba_2Ca_{0.67}M_{0.33}NbO_{6-\delta}$ (M = Mn, Fe, Co). The calculated μ_{eff} and number of unpaired electrons were also shown in the inset.

Figure 8. (a) Structure of double perovskite-type $Ba_2Ca_{0.67}M_{0.33}NbO_{6-\delta}$ (M = Mn, Fe, Co) and (b) bond valence sum map shows the low bond valence unit (u.v. = 0.4) mismatch contour plot (light yellow) of O^{2-} ions. (c) Slice through a geometry-optimized 2×2×3 supercell of $Ba_2Ca_{0.67}Co_{0.33}NbO_{5.5}$ with three superimposed isosurfaces of constant bond valence site energy. The thickness of the displayed slice is restricterd one unit cell in order to minimize overlap of pathway regions. The dark, medium and light isosurfaces correspond to energies characteristic of equilibrium sites (0.05 eV), localized pathways

within NbO_x coordination polyhedra (0.25 eV) and the energy at which a percolating pathway for long-range O^{2-} motion is formed (0.7 eV), respectively.

Figure 9. Arrhenius plot of the oxide ion conductivity determined from the mean square displacement of oxide ions in NVT molecular dynamics simulations of $Ba_{96}Ca_{32}Co_{16}Nb_{48}O_{264}$ assuming validity of the Nernst-Einstein relationship (filled symbols) yields an activation energy of 0.69 eV for long range oxide ion motion for temperatures ≥ 800 K. The limiting slopes of mean-square displacement curves for lower temperatures and slopes over intermediate time domains for the higher temperatures correspond to localized oxide ion hops within NbO_x coordination polyhedral that occur with a considerably lower activation energy of ca. 0.24 eV (crosses). Straight lines are linear regressions of the displayed data as a guide to the eye.

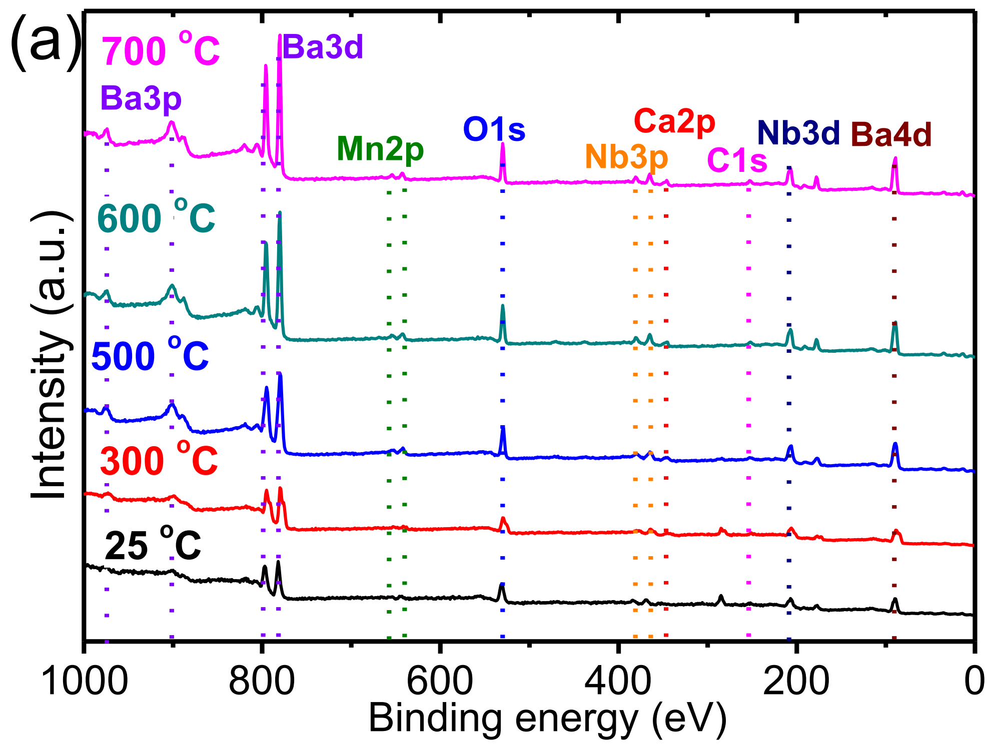

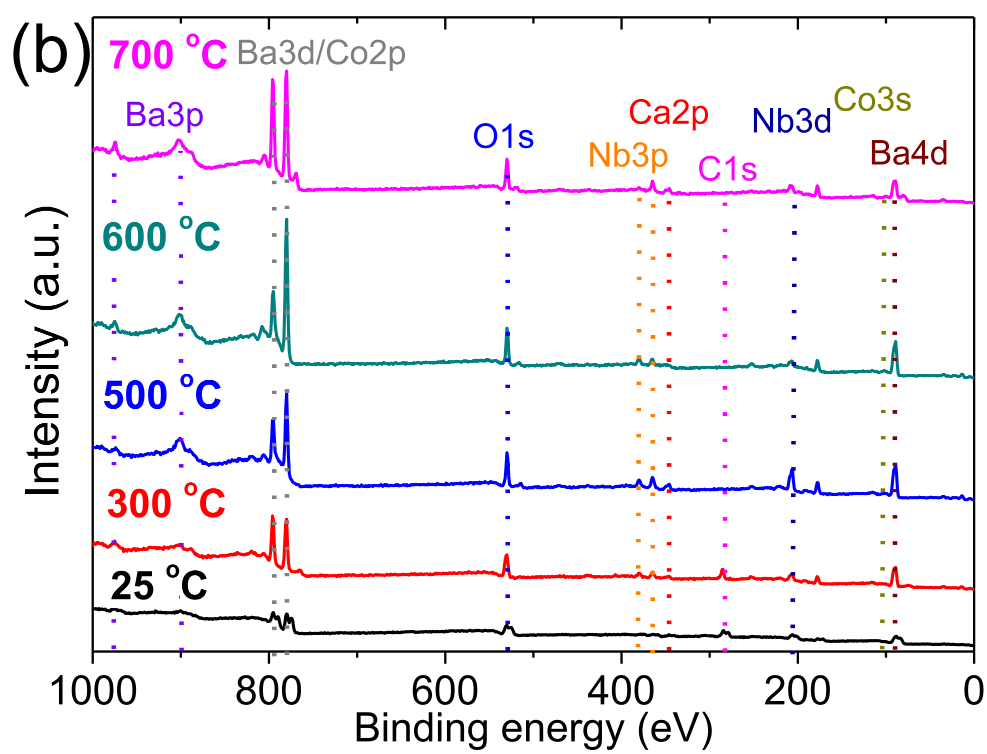

Figure 1. X-ray photoelectron spectroscopy (XPS) elemental analysis of the near-surface of (a) $Ba_2Ca_{0.67}Mn_{0.33}NbO_{6-\delta}$ and (b) $Ba_2Ca_{0.67}Co_{0.33}NbO_{6-\delta}$ from 25-700 °C.

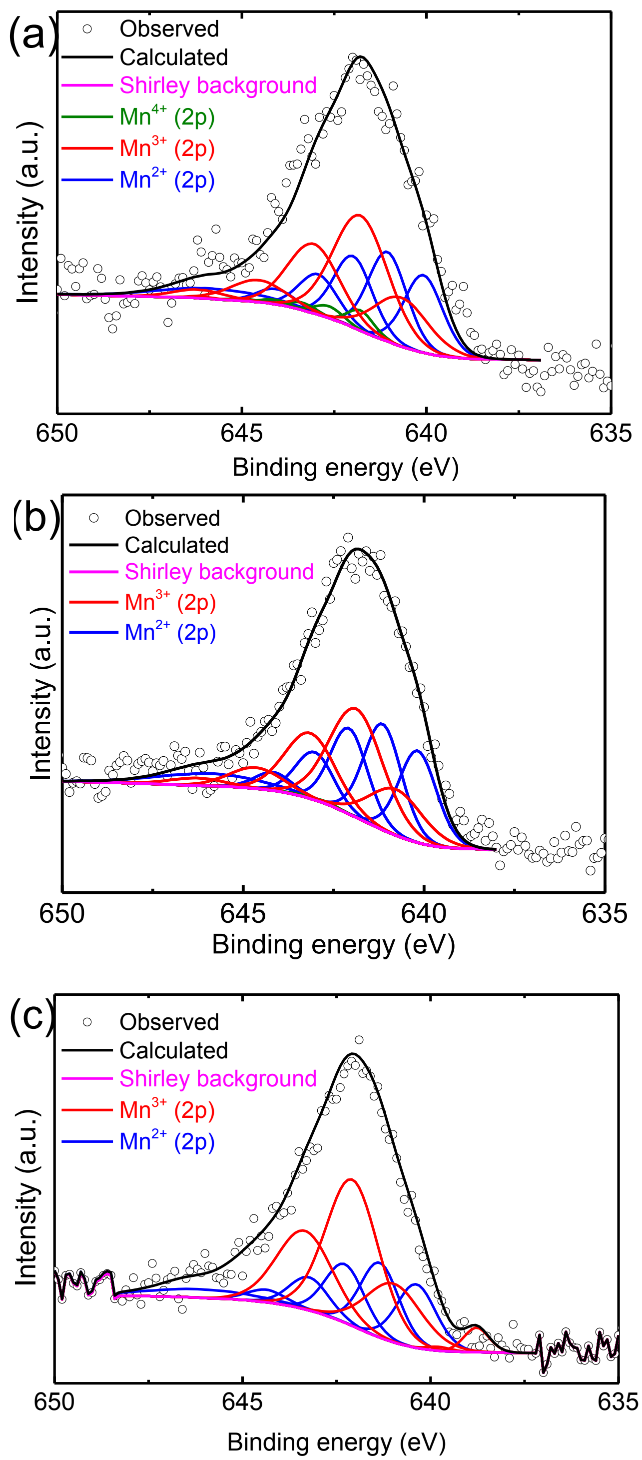

Figure 2. Multiplet curve-fitting of Mn $2p_{3/2}$ spectra at (a) 500 ^{o}C, (b) 600 ^{o}C and (c) 700 ^{o}C.

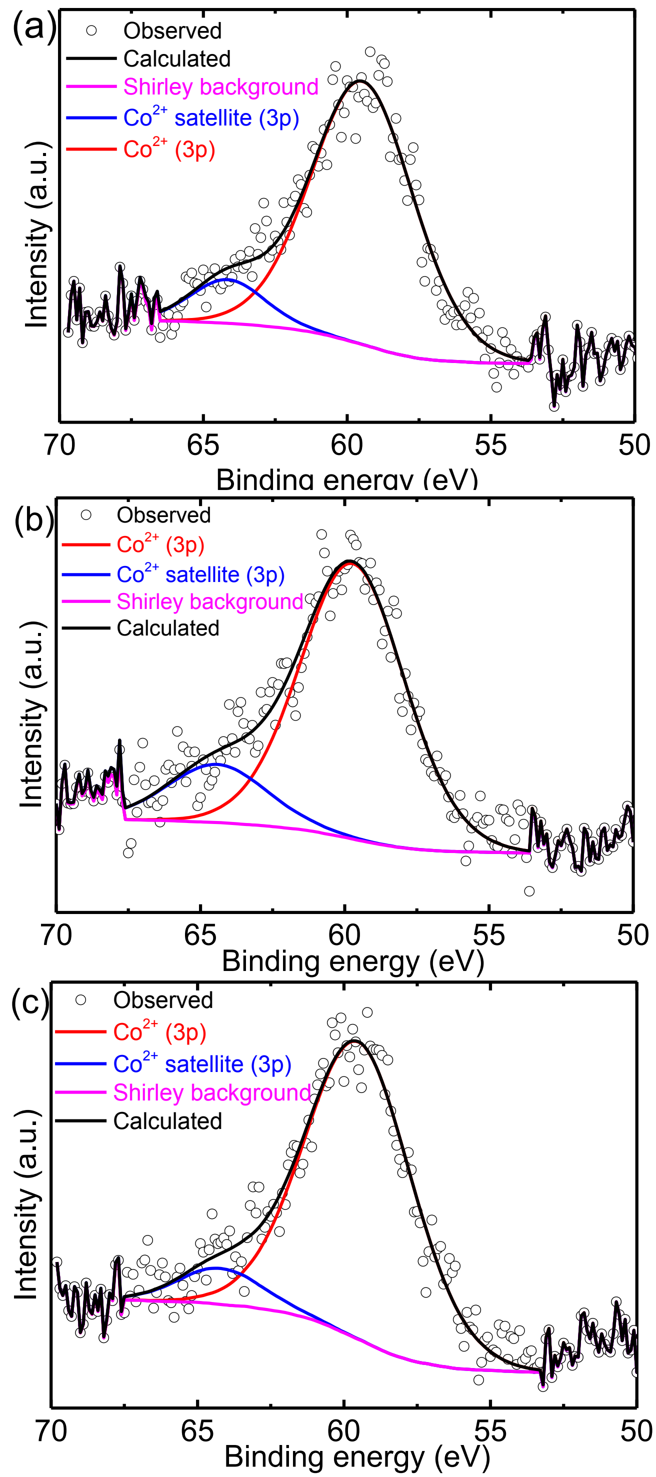

Figure 3. Curve-fitting of Co^{2+} $3p_{3/2}$ spectra at (a) 500 ^{o}C, (b) 600 ^{o}C and (c) 700 ^{o}C of $Ba_2Ca_{0.67}Mn_{0.33}NbO_{6-\delta}$.

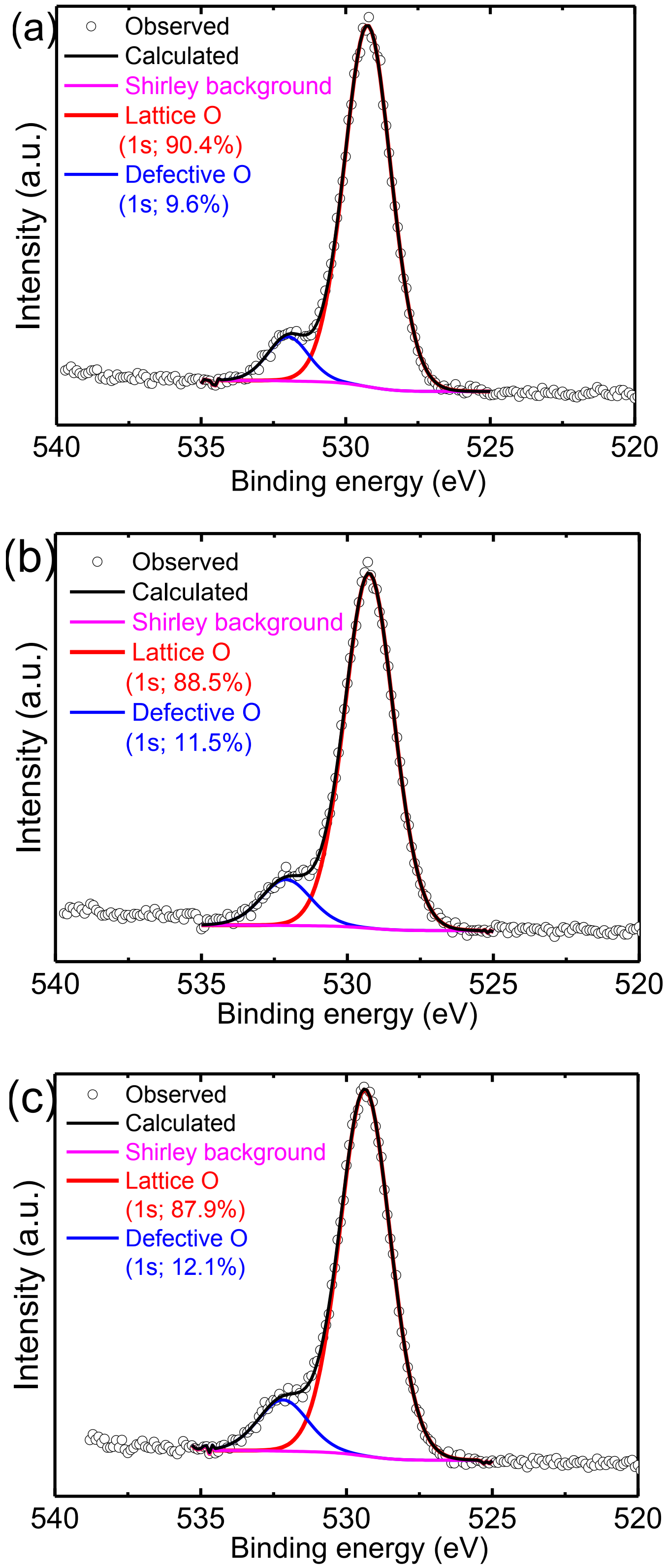

Figure 4. Curve-fitting of O $1s_{1/2}$ spectra at (a) 500 °C, (b) 600 °C and (c) 700 °C of $Ba_2Ca_{0.67}Co_{0.33}NbO_{6-\delta}$.

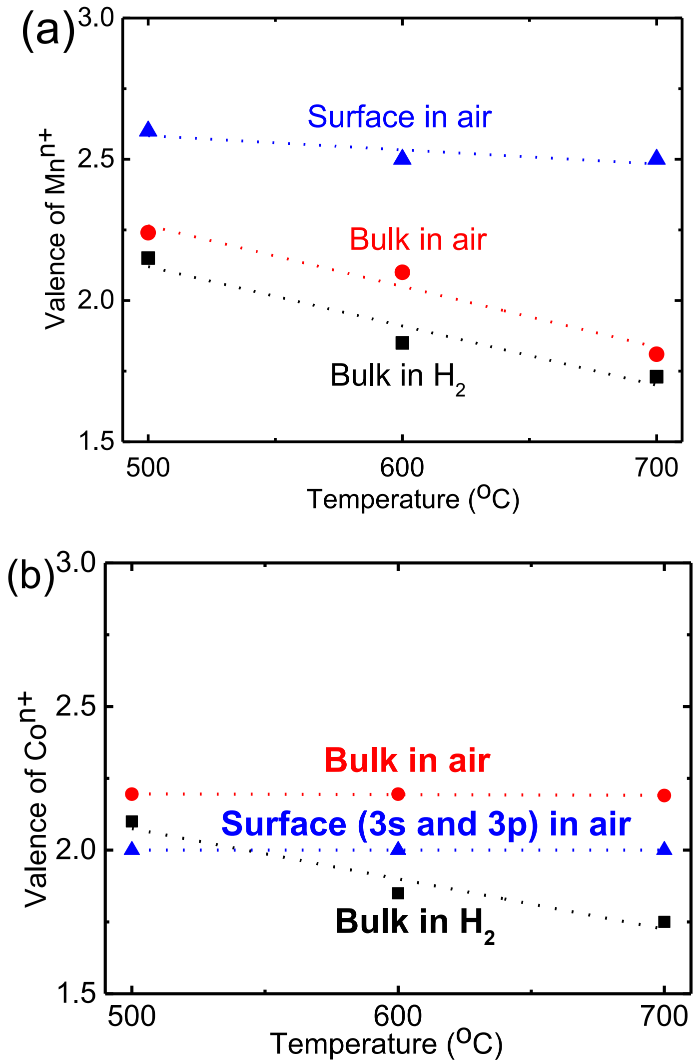

Figure 5. Bulk (air and H_2) and surface (air) valences of (a) $Ba_2Ca_{0.67}Mn_{0.33}NbO_{6-\delta}$ and (b) $Ba_2Ca_{0.67}Co_{0.33}NbO_{6-\delta}$ from 500-700 °C.

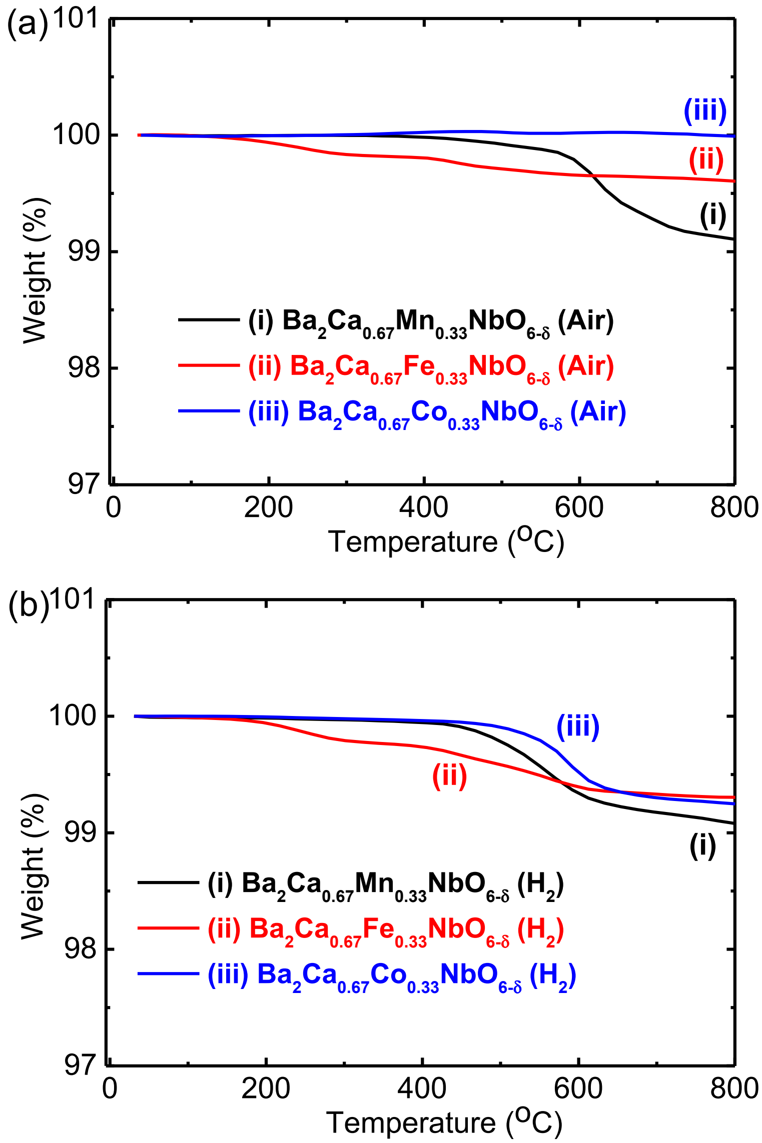

Figure 6. Thermogravimetric analysis (TGA) of $Ba_2Ca_{0.67}M_{0.33}NbO_{6\text{-}\delta}$ (M = Mn, Fe, Co) in air (a) and H_2 (b).

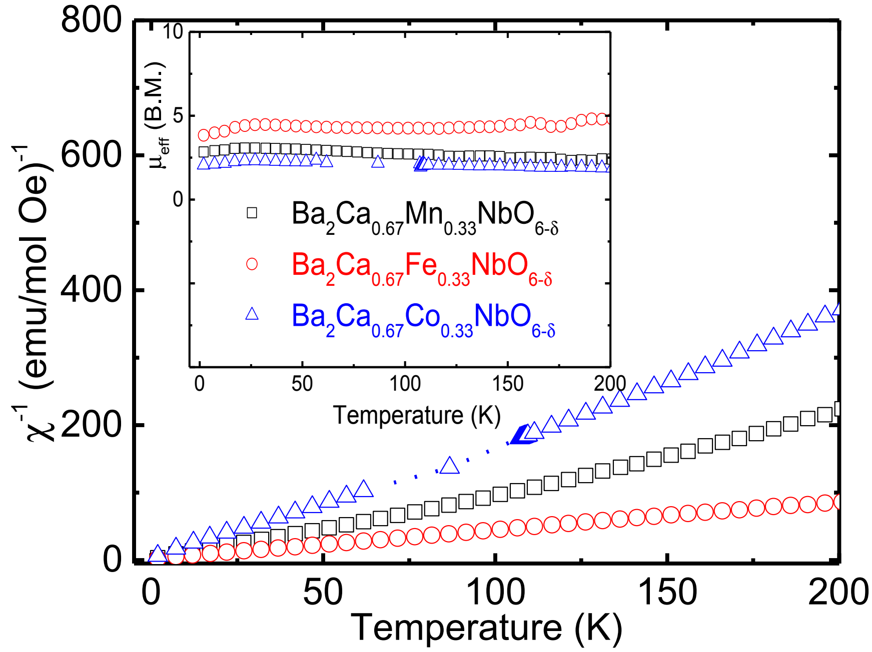

Figure 7. Field-cooled (FC) measurements for powdered samples of $Ba_2Ca_{0.67}M_{0.33}NbO_{6-\delta}$ (M = Mn, Fe, Co). The calculated μ_{eff} and number of unpaired electrons were also shown in the inset.

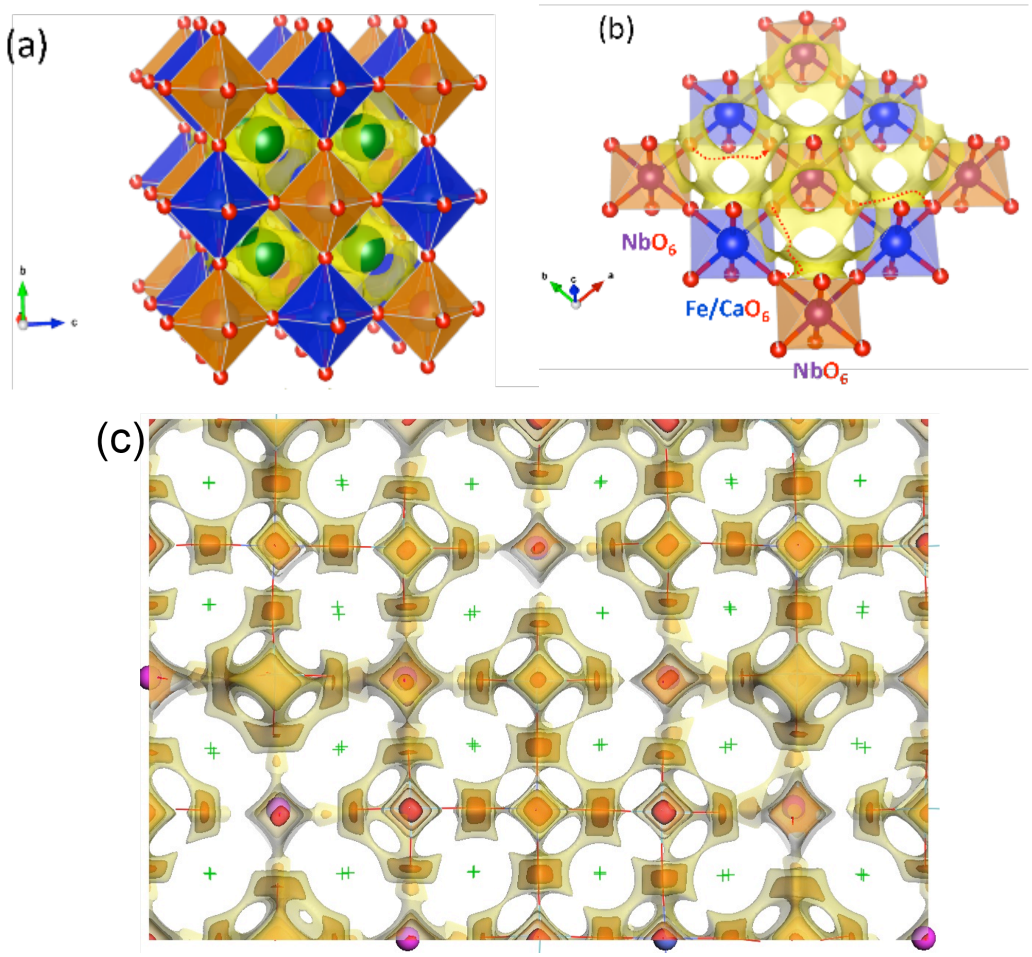

Figure 8. (a) Structure of double perovskite-type $Ba_2Ca_{0.67}M_{0.33}NbO_{6-\delta}$ (M = Mn, Fe, Co) and (b) bond valence sum map shows the low bond valence unit (u.v. = 0.4) mismatch contour plot (light yellow) of O^{2-} ions. (c) Slice through a geometry-optimised 2×2×3 supercell of $Ba_2Ca_{0.67}Co_{0.33}NbO_{5.5}$ with three superimposed isosurfaces of constant bond valence site energy. The thickness of the displayed slice is restricterd one unit cell in order to minimize overlap of pathway regions. The dark, medium and light isosurfaces correspond to energies characteristic of equilibrium sites (0.05 eV), localized pathways within NbO_x coordination polyhedra (0.25 eV) and the energy at which a percolating pathway for long-range O^{2-} motion is formed (0.7 eV), respectively.

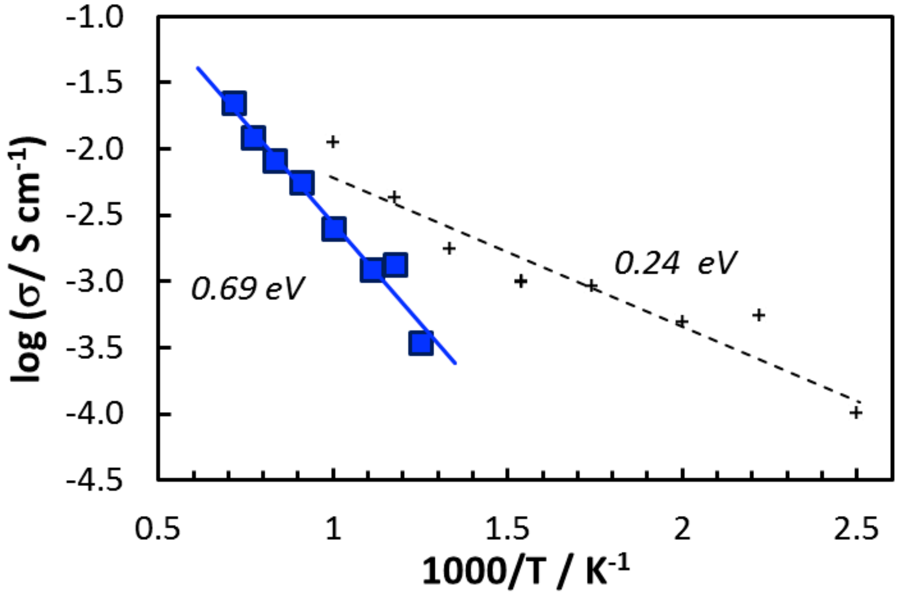

Figure 9. Arrhenius plot of the oxide ion conductivity determined from the mean square displacement of oxide ions in NVT molecular dynamics simulations of $Ba_{96}Ca_{32}Co_{16}Nb_{48}O_{264}$ assuming validity of the Nernst-Einstein relationship (filled symbols) yields an activation energy of 0.69 eV for long range oxide ion motion for temperatures ≥ 800 K. The limiting slopes of mean-square displacement curves for lower temperatures and slopes over intermediate time domains for the higher temperatures correspond to localized oxide ion hops within NbO_x coordination polyhedral that occur with a considerably lower activation energy of ca. 0.24 eV (crosses). Straight lines are linear regressions of the displayed data as a guide to the eye.

For Table of Content Only

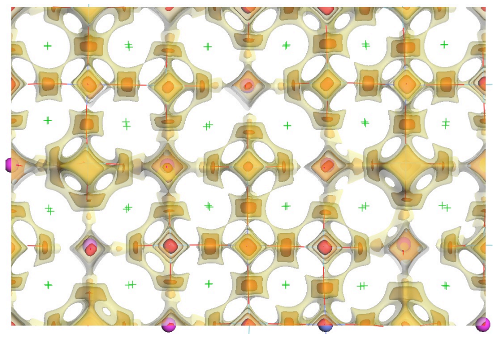

TOC abstract: Surface valence, magnetic ordering and oxide-ion transport properties of $Ba_2Ca_{0.67}M_{0.33}NbO_{6-\delta}$ (M = Mn, Fe, Co)